ACS NANO

www.acsnano.org

ARTICLE

Anomalous Glide Plane in Platinum Nano- and Microcrystals

Marie-Ingrid Richard,* Stéphane Labat, Maxime Dupraz, Jérôme Carnis, Lu Gao, Michaël Texier, Ni Li, Longfei Wu, Jan P. Hofmann, Mor Levi, Steven J. Leake, Sergey Lazarev, Michael Sprung, Emiel J.M. Hensen, Eugen Rabkin, and Olivier Thomas

Cite This: https://doi.org/10.1021/acsnano.3c01306

Read Online

ACCESS | Metrics & More | Article Recommendations

ABSTRACT: **At the nanoscale, the properties of materials depend critically on the presence of crystal defects. However, imaging and characterizing the structure of defects in three dimensions inside a crystal remain a challenge. Here, by using Bragg coherent diffraction imaging, we observe an unexpected anomalous {110} glide plane in two Pt submicrometer crystals grown by very different processes and having very different morphologies. The structure of the defects (type, associated glide plane, and lattice displacement) is imaged in these faceted Pt crystals. Using this noninvasive technique, both plasticity and unusual defect behavior can be probed at the nanoscale.**

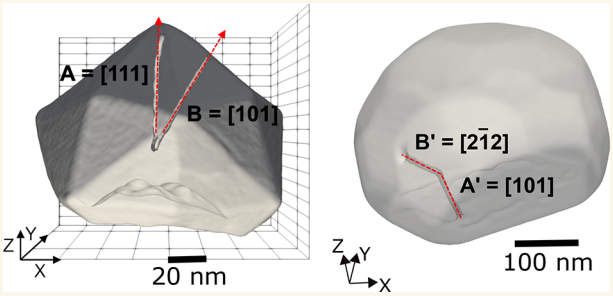

KEYWORDS: *glide planes, dislocations, platinum, Bragg coherent diffraction imaging, defects*

INTRODUCTION

In face centered cubic (fcc) metals, plasticity is generally thought to occur by the motion of dislocations in well-defined planes and directions. These groupings of planes and directions are called slip systems and are the conventional way of describing plastic deformation caused by dislocation slip. In fcc metals, slip generally occurs on {111} planes in <110> directions.[1,2] The perfect Burgers vector, **b**, is $\frac{a}{2}\langle 110\rangle$ (a being the lattice unit), which is a close packed direction, and represents the shortest repeat length in the crystal. Other uncommon slip planes are sometimes encountered in fcc crystals,[2] for example: {100}, {110}, {121} or {212}. They are either observed at elevated temperatures ({100},[3] {110}[4] or {212}[5]) or on deformed specimens ({100},[6,7] {110}[8] or {121}[9]). These nonoctahedral slip planes may result through cross-slip in the <110> direction.[1] As defects have a critical influence on the properties and performances of materials, it is critical to establish the fundamental slip planes for crystal plasticity models. Most of the experimental observations on slip planes have been performed on bulk crystals. The energy and mobility of defects in single nano-objects may be different compared to their bulk counterparts due to surface effects.[10] At the nanoscale, the number of defects (*e.g.*, dislocations) in a crystal is reduced and their behavior cannot be determined by a statistical approach. Crystal defects are not always detrimental for performances as they can instead give rise to specific functionalities, such as improving adsorption affinity or enhancing the catalytic activity.[11−13] However, quantifying the lattice distortions associated with defects as well as imaging the structure of defects in three-dimensions (3D) are challenging at the nanoscale. Accurate identification of the dislocation line, slip planes as well as the knowledge of the strain at the scale of defects are essential to the understanding of fundamental defect behaviors and the underlying physics.

To investigate defects and associated slip planes in small objects, we employed a noninvasive technique called Bragg Coherent Diffraction Imaging (BCDI).[14] BCDI is a lensless imaging technique based on inverse microscopy, which employs highly accurate digital methods to replace the X-ray imaging lenses. This technique combines 3D coherent diffraction measurements of Bragg peaks and phase retrieval algorithms to obtain a spatial reconstruction of individual nanoscale objects. The technique is sensitive to atomic displacement and strain. The retrieved object in direct space is a complex field, whose modulus encodes the electron density

Received: February 10, 2023
Accepted: March 7, 2023

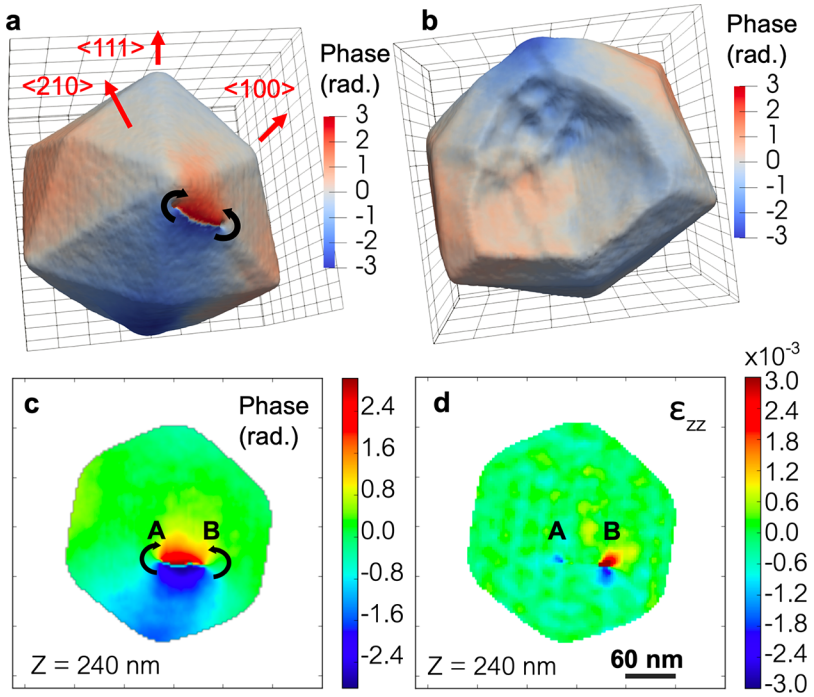

Figure 1. Phase and out-of-plane strain of the reconstructed THH Pt crystal. (a) Top and (b) bottom views of the isosurface of the reconstructed phase (in radians) of the Pt particle drawn at 35% of the maximum density. The amplitude is used to draw the isosurface, while the phase is projected onto the isosurface as the colormap. The black and red arrows indicate a phase defect and directions, respectively. The 3D grid has a spacing of 50 nm in Figures (a) and (b). (c)-(d) Two-dimensional cut of the phase and out-of-plane strain, ϵ_{zz}, at a particle height of 240 nm, respectively.

$\rho(\mathbf{r})$ of the object, and its phase, the displacement field $\mathbf{u}(\mathbf{r})$ projected onto the diffraction vector. The displacement field information is crucial in identifying the character of single dislocations. Thanks to the high brilliance, coherence, and flux of synchrotron X-ray beams, BCDI has shown its capability to image single defects in nanocrystals[12,15−19] together with an unmatched sensitivity (picometer resolution) to displacement fields.[16] BCDI can be used to understand the impact of buried single defects on properties under *in situ* conditions.[12,19]

Here, we apply BCDI to image and characterize in 3D the structure of defects in single faceted platinum (Pt) crystals. A {110}-type glide plane has been observed in two Pt crystals prepared *via* a chemical and physical process. This paper presents evidence for this anomalous nonoctahedral glide plane in fcc submicrometer crystals. The {110} slip plane is associated with preferential nucleation of defects at the surface of the crystals. Noninvasive structural characterization of defects allows understanding defect behaviors in confined crystals and will facilitate defect engineering to enhance material performances.

RESULTS

Two types of Pt particles have been prepared *via* a chemical (electrochemical deposition and faceting) and a physical (dewetting) process. For both samples, a high proportion of perfect (defect free) particles are observed. In this paper, we will concentrate on defective particles. The two crystals measured here are a tetrahexahedral (THH) Pt particle grown on a glassy carbon substrate[20] by electrodeposition and faceting and a dewetted Pt particle epitaxially grown on a sapphire substrate (see Experimental Section). The three-dimensional BCDI measurements were performed by measuring the scattered intensity in the vicinity of the specular **111** Pt Bragg reflection at the ID01 beamline of the European Synchrotron (ESRF) and at the P10 beamline of PETRA III synchrotron. Experimental details are given in the Experimental Section. The reconstructed density and phase are displayed with a voxel size of 3 nm^3 (3.5 nm^3) for the THH Pt particle (dewetted Pt particle). The resolution of the reconstruction is estimated to 18.3 nm (THH Pt particle) and 27 nm (dewetted Pt particle) using the Phase-Retrieval Transfer Function (PRTF),[21,22] which measures how well the retrieved Fourier amplitude matches the square root of the measured diffraction intensity. Details about the phase retrieval process are described in the Experimental Section. The phase map obtained from the inversion of the BCDI measurement at the **111** Bragg reflection encodes the displacement field, u_{111}, along the [111] direction, which is normal to the substrate surface (either glassy carbon for the THH particle or sapphire for the dewetted particle).

Figure 1 shows the reconstructed phase (proportional to u_{111}) and strain (ϵ_{111}) fields of the THH crystal. The isosurface of the reconstructed Pt particle is drawn at 35% of the maximum electron density for the (a) top and (b) bottom views. The particle is strongly faceted with {201} planes, which correspond to high-index facets of the THH shape.[20] Discontinuities appear in the reconstructed phase field as indicated by black arrows in Figures 1(a) and (c). They are the signature of defects within the crystallite. They are observed as a line in the phase plot, which can be described as a sharp phase boundary ended by 2π phase vortices (region where the phase varies from $-\pi$ to π). The two phase vortices are the signature of two dislocation cores. The phase jump in the reconstruction links the two dislocations (see Figures 1(a)-(c)), suggesting that they consist of two ends of the same dislocation line. The strain has been derived from the

https://doi.org/10.1021/acsnano.3c01306
ACS Nano XXXX, XXX, XXX−XXX

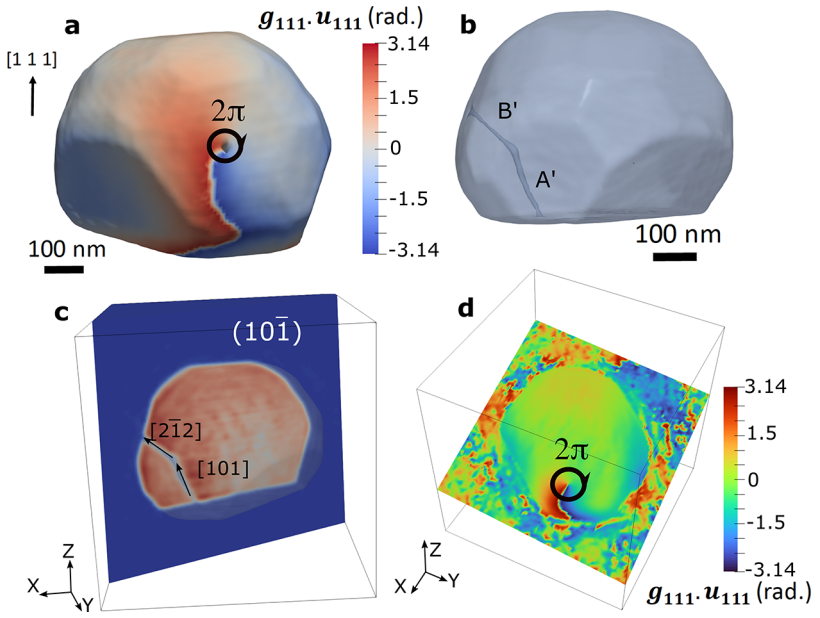

Figure 2. Phase and modulus of the reconstructed dewetted Pt crystal. Reconstructed (a) phase and (b) modulus. Slice of the reconstructed modulus (c) and phase (d). The isosurface is drawn at 35% of the maximum electron density.

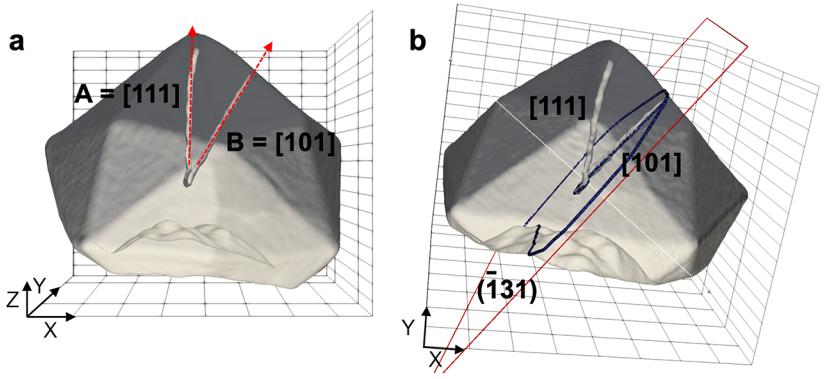

Figure 3. Dislocation loop and possible slip planes of the Pt THH particle. (a) Wireframe plots of the reconstructed electron density of the Pt particle drawn at 35% of the maximum density. The direction of the two segments of the dislocation loop is evidenced. (b) Visualization of the plane containing the [101]-segment and the curved junction toward the [111]-segment. The 3D grid has a spacing of either 20 nm (along Z in Figure a) or 50 nm.

displacement field: $\epsilon_{zz} = \frac{\partial u_{111}}{\partial z}$ and using the procedure described in ref.[23] (see Figure 1(d)). Note that the out-of-plane ϵ_{zz} strain is different around the two segments (labeled as **A** and **B**) of the dislocation, implying that they are of different types. Figure 2 shows the reconstructed phase and modulus (*i.e.*, electron density) of the dewetted Pt crystal. The isosurface is drawn at 35% of the maximum electron density. As well, a discontinuity appears in the reconstructed phase field (see Figure 2(a)), which is the signature of a dislocation. Note that for the dewetted Pt particle, the dislocations appear pinned at the free surface as well as at the Pt/substrate interface (see Figure 2(b)).

Different methods have been applied to determine the dislocation lines after phase retrieval, like derivative-based method[24] for dislocation core and/or guided algorithms[25,26] (min-max optimization formulation). Here, the 3D dislocation line orientation is determined using the spatial amplitude variation of the retrieved density/modulus (see Figures 2(b) and 3). Simulations of defects in BCDI have shown low amplitude along the dislocation line.[25] Large lattice strains near the dislocation core lead to scattered intensity beyond the numerical aperture of the detector, resulting in a loss of amplitude at the dislocation core. In Figures 2(b) and 3, line contours are observed, which appear as regions or pipes of lower density. The spatial modulus variation is the signature of dislocations, which is made of two segments (labeled **A** and **B**) for the Pt THH crystal (see Figures 1 and 3) and also of two segments (labeled **A′** and **B′**) for the Pt dewetted crystal (see Figure 2(b)). It was possible to index the direction of the two segments courtesy of the scattering vector **g** (here, **111** Bragg reflection) and the different types of facet of the crystal: {201}-type facets for the THH Pt particle and low-index {001}, {110} and {111} facets for the dewetted Pt particle. For the Pt THH particle, the segment **A** is along [111] and segment **B** is along either [110], [011] or [101]; we arbitrarily fix its direction to [101]. For the Pt dewetted crystal, the segment **A′** is along [101] and the segment **B′** is along a ⟨2 $\bar{1}$2⟩-type direction (here, arbitrarily fixed to [2 $\bar{1}$2]). Note that the [111]-segment of the dislocation loop of the Pt THH particle is not perfectly straight. As observed in Figure 3(a), it is

https://doi.org/10.1021/acsnano.3c01306
ACS Nano XXXX, XXX, XXX−XXX

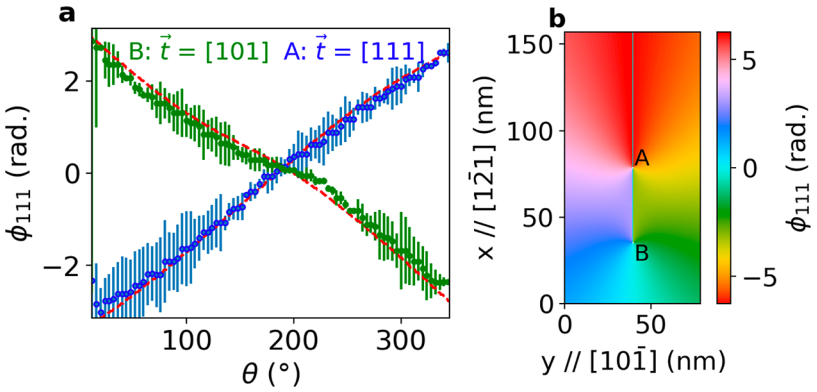

Figure 4. Phase evolution around segments. (a) Reconstructed and simulated (red dashed lines) phase as a function of azimuthal coordinate θ for segments A and B of the THH Pt particle. The error bars correspond to the observed variation of the phase over a distance of 25 nm from the center of each defect. (b) Superposition of the ϕ_{111} phase of the two segments supposing a common Burgers vector ($\frac{a}{2}$[101]), which is along the dislocation line of the B segment ($\vec{t}$ = [101]).

slightly curved close to the crystal surface. The plane containing the [101]-segment and the curved junction toward the [111]-segment is a $(\bar{1}31)$ plane, meaning that the dislocation loop rotates in a $(\bar{1}31)$ plane. For the Pt dewetted particle, the two ([101] and [2 $\bar{1}$2]) segments lie in a (10 $\bar{1}$) plane (see Figure 2(c)). Note that the spatial resolution of the BCDI is not sufficiently high to observe a possible dissociation of the dislocations.

DISCUSSION

The {111}-type plane is the major operative slip system in fcc structures, as the {111} planes are the most densely packed planes in fcc metals, like Pt.[2] For the Pt THH particle, the **A** segment is along the [111] direction and, thus, cannot lie in a {111} plane. Also, for the Pt dewetted particle, the **A′** segment is along the [2 $\bar{1}$2] direction and, thus, cannot lie in a {111} plane. The configuration of these two defects is unexpected in fcc metals.

Note that here, we concentrated on a single crystal reflection, **g** = 111. This provides only one component of the lattice displacement field. A dislocation gives rise to diffraction contrast if **g**·**b** is nonzero.[27,28] This means that X-rays are sensitive to a dislocation if the displacement field generated by the dislocation has a nonzero projection onto the particular Bragg peak. Possible Burgers vectors in face centered cubic materials (like, Pt) are $\frac{a}{2}\langle 110\rangle$ or $\langle 100\rangle$. In our case, as **g** = 111, dislocation lines with a Burgers vector of type $[1\bar{1}0]$, $[10\bar{1}]$ or $[01\bar{1}]$, for instance, can not be measured as they are invisible for this condition (**g**·**b** = 0). To get the full picture of the defects as well as the full lattice displacement and strain fields, measurements of at least three (independent) nonco-linear reflections are needed.[16,29] Nevertheless, as in the two particles, one segment of the measured dislocations is along a direction (either [111] or [2$\bar{1}$2]) that cannot lie in a {111} plane; with only one reflection, we can assert that the configuration of the defects in the two particles is unusual in fcc.

For the Pt dewetted particle, the glide plane of the two (**A′** and **B′**) segments can be determined straightforwardly as the segments lie in a (10 $\bar{1}$) plane (see Figure 2). This implies that the glide plane of the defects corresponds to an anomalous {110}-type plane. For the THH particle, a single plane can not contain the two segments as well as its junction, it is then necessary to determine the Burgers vector and the type (screw, edge or mixed) of the two main segments of the dislocation to estimate their possible glide planes. As we know the direction of the dislocation line of the **A** segment ($\vec{t}$ = [111]) and that in fcc crystals, the Burgers vector is either $\frac{a}{2}\langle 110\rangle$ or $\langle 100\rangle$, the only possible glide plane for the **A** segment, that fulfills $\vec{b}\otimes\vec{t}$, is of {110}-type. Interestingly, for both the dewetted and THH Pt particles, an anomalous {110}-type glide plane is observed.

To determine the type (screw, edge or mixed) of the two (**A** and **B**) main segments of the dislocation in the Pt THH particle, we investigated the reconstructed phase and displacement field, u_{111}, around the two segments. It gives a continuum description of how the atoms are displaced from their equilibrium positions and gives insight of the nature of the dislocation loop. Figure 4(a) shows the reconstructed phase along the [111] direction as a function of azimuthal angle, θ, for segments **A** and **B**. For segment **A**, the phase, proportional to u_{111}, varies quasi-linearly around the segment (shift of 2π over 360°). For segment **B**, periodic modulations of the phase are observed as a function of θ. If we consider a screw dislocation along the z-direction in a cubic crystal and in an isotropic infinite media (the Zener or elastic ratio for Pt being equal to 1.6, this implies that Pt is close to an isotropic elastic media), then the displacement field is given by[2]

$$u_z(r,\theta) = b\frac{\theta}{2\pi} \tag{1}$$

where b is the modulus of the Burgers vector and θ measures the angle around the dislocation core. As the phase corresponds to $\mathbf{g}_{111}\cdot\mathbf{u}(\mathbf{r})$ (where $\mathbf{g}_{111}$ is the scattering vector at the **111** Pt Bragg reflection), a linear variation of the displacement field leads to a linear variation of the phase. The phase around the **A** segment varies quasi-linearly. This demonstrates that the dislocation should have a screw component along the [111] direction. An edge component of the **A** segment may exist but can not be detected. As only the **g** = **111** reflection has been measured, the edge component is invisible for this condition. The **A** segment is then the screw component of a mixed dislocation with a Burgers vector of type **b** = $\frac{a}{2}\langle 110\rangle$ or $a\langle 001\rangle$ (the two possible Burgers vectors in fcc). For these two Burgers vectors, the phase, $\phi(\theta)$, will vary linearly, as experimentally observed (see Figure 4(a)) since $\mathbf{g}_{111}\cdot\mathbf{u}(\mathbf{r})$ equals to θ ($g_{111} \times u_{110} \times \cos(\beta)$ =

https://doi.org/10.1021/acsnano.3c01306
ACS Nano XXXX, XXX, XXX−XXX

$\frac{2\pi\sqrt{3}}{a} \times b_{110}\frac{\theta}{2\pi} \times \cos(\beta) = \theta$, with $b_{110} = \frac{a}{\sqrt{2}}$ and β, being the angle between the [111] and [110] directions; or $g_{111} \times u_{100} \times \cos(\beta) = \frac{2\pi\sqrt{3}}{a} \times b_{100}\frac{\theta}{2\pi} \times \cos(\beta) = \theta$, with $b_{100} = a$ and β, being the angle between the [111] and [100] directions). The **B** segment shows a 2π-modulation. It cannot be an edge dislocation as a π-modulation of the phase around the dislocation core should be observed. As the two **A**and **B** segments are close together inside the crystal, we simulated the superposition of the out-of-plane displacement (u_{111}) and phase (ϕ_{111}) of the two segments supposing a common Burgers vector ($\frac{a}{2}$[101]), which is along the dislocation line of the **B** segment ($\vec{t}$ = [101], see Figure 4(b)). As the two lines emerge at the sample surface, they are connected and must have the same Burgers vector. In this case, **A** and **B** segments are a mixed dislocation ($\vec{t}$ = [111] and $\vec{b} = \frac{a}{2}$[101]) and a screw dislocation ($\vec{t}$ = [101] and $\vec{b} = \frac{a}{2}$[101]), respectively. Interestingly, this defect configuration reproduces quite well the observed variations of the phase around the two segments (Figure 4(a)). Thus, the **A** segment is lying in an anomalous (10 $\bar{1}$) glide plane, while it is highly probable that the **B** segment is lying in a (111)-type glide plane. Here, a single reflection allows us to unambiguously characterize the two segments (type and Burgers vector) by measuring and simulating the displacement field around them.

The unusual glide plane observed for the **A** segment in the THH Pt particle can be (1) a pure ⟨110⟩ {110} slip system, *i.e.* induced by emission of dislocations from sources lying in {110} planes, (2) the consequence of cross-slip from ⟨110⟩ {111} to ⟨110⟩ {110} or (3) a zigzag configuration, *i.e.* that the observed line lies in {111} planes at a small scale (at the limit of our resolution) with a mean direction parallel to the trace of {110} planes. The latter case may be ruled out, as it has been observed that zigzag dislocations exhibit cross-slip events separated by distance generally larger than our spatial resolution (10 nm).[30−32] The second hypothesis can also be ruled out, as it is energetically unfavorable to cross-slip from {111} planes into {110} planes. Note that it has been observed that high temperature and high stacking-fault energy like in Pt may reduce the energy necessary for the crossing from {111} to {110}.[32] In our case, the hypothesis of a pure <110> {110} glide is the most probable. The nonoctahedral {110} slip planes are unusual in fcc metals, but they have been observed in particular conditions: (1) compression tests at high temperature,[4] (2) deformation experiments on Al single crystals,[33] (3) high speed deformation experiment on Al,[8] and (4) in slightly deformed (±1.2 MPa) Cu single crystals at room temperature.[32] In the latter case, the high perfection of the crystal and the activation of surface sources may explain the possibility of pure {110} slip plane. Indeed, in this case, the pure {110} slip plane was associated with preferential surface nucleation as influenced by image forces. Image forces become significant when a dislocation is close to a surface. A pure {110} slip plane can thus be encountered in nanostructures in contrast to bulk fcc materials as free surfaces can favor surface nucleation in {110} planes as observed in ref.[32]

For the Pt dewetted particle, the two segments lie in a (10$\bar{1}$) plane. As the particle has been formed after dewetting at high temperature (1000 °C), it is possible that the dislocations form at high temperature during the cooling process (thermal stress) as slip in {110} planes is known to be thermally activated.[34]

Several groups have observed a nonoctahedral slip in Pt in the past and during deformation (see for examples, refs.[6,35]). It coincides with the {100}⟨011⟩ slip system. Here, a {110} slip system is observed. The thermal stress is mainly a shear parallel to the substrate, and this may act differently on the particle as compared to a normal compression/deformation. The surface nucleation barriers probably play a decisive role here. The Pt dewetted particle has been annealed at 450 °C and under different gas conditions. As shown in Figure 5, we observed no

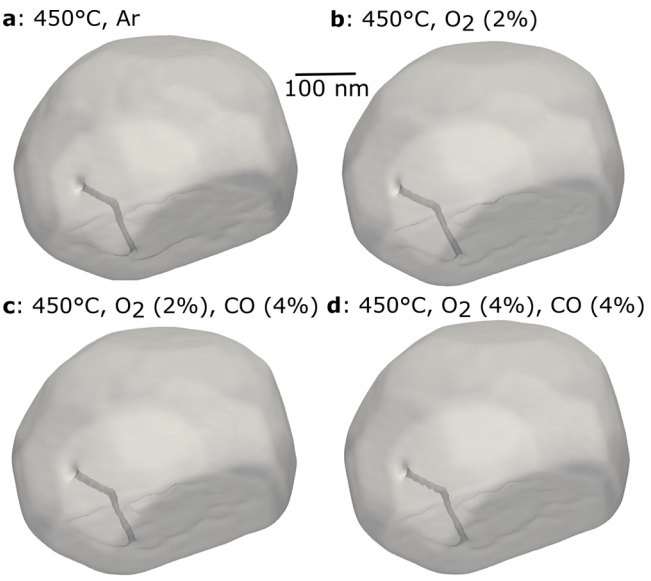

Figure 5. Under gas conditions. Reconstructed modulus of the reconstructed dewetted Pt crystal annealed at 450 °C under (a) Ar, (b) O_2 (4%), (c) O_2 (2%) and CO (4%) and (d) O_2 (4%) and CO (4%).

movement of the two segments upon heating of the particle to 450 °C and under different gases. This stability can be explained by the fact that the dislocations have been formed at a higher temperature (dewetting at 1000 °C). Note that unseen defects, verifying the invisibility condition at the **111** Bragg reflection, may also explain the stability of the two segments in the particle. As discussed above, for the Pt THH particle (growth at room temperature), it is thus highly possible that the **A** segment (along [111]) lies in a pure {110} slip plane. Then, the junction and **B** segment (along [101]) may result from cross-slipping from {110} into {111} and heterogeneous cross-slipping from a {111} plane into another {111} plane, respectively, as it is energetically favorable to cross-slip into {111} planes. The junction being located at the center of the particle, this region has a different atomic environment/stress state that could facilitate the cross-slip.

Conclusions. In summary, we measure the 3D displacement field in single Pt particles using BCDI. The technique enables a characterization of the 3D morphology of defects. Our results shed light on anomalous glide {110}-type planes in platinum crystals. Two Pt particles prepared either via a chemical or a physical process and having very different morphologies show dislocations in {110} glide planes. The {110} slip plane is associated with preferential nucleation of defects at the surface of the nanostructures. More studies will be needed to generalize this phenomenon for other fcc nanostructures. BCDI will allow 3D structural visualization of dislocations under external conditions like heterogeneous

https://doi.org/10.1021/acsnano.3c01306
ACS Nano XXXX, XXX, XXX−XXX

catalytic gas phase, temperature or mechanical force changes and will facilitate strain and defect engineering.

EXPERIMENTAL SECTION

Sample Preparation. The tetrahexahedral (THH) Pt particles were electrochemically synthesized on glassy carbon (GC) electrodes by a square-wave-potential method with a saturated calomel reference electrode (SCE) and a Pt foil counter electrode in 2 mM H_2PtCl_6 and 0.1 M H_2SO_4 electrolyte following the procedure in ref.[20] The GC electrode is first subjected to a potential of +1.20 V for 2 s to clean the surface and then −0.35 V for 60 ms to create Pt nuclei. The Pt nuclei grows to THH particles by applying a square-wave-potential between +0.04 V and +1.09 V at 100 Hz for 10 min. In the case of the dewetted Pt particles, a 30 nm thick Pt film was deposited on sapphire with an electron beam evaporator. The Pt nanocrystals have their *c*-axis oriented along the [111] direction normal to the (0001) Al_2O_3 substrate. A standard photolithography method was employed to prepare a patterned layer of photoresist on sapphire prior to the electron beam evaporation of Pt. The lithographic processing route ensured that a number of dewetted Pt particles are well-separated from their neighbors and that only one crystallite is irradiated by the incoming X-ray beam. The diameter of the particles ranges between 200 and 600 nm.

Experimental Setup. The X-ray experiments were carried out at the upgraded ID01 beamline of the ESRF synchrotron and at the P10 beamline of PETRA synchrotron. At the ID01 beamline, the beam size was focused down using a Fresnel zone-plate (FZP). The resulted beam size was about 310 nm (horizontally) × 170 nm (vertically). A coherent portion of the monochromatic X-ray beam was selected with high precision slits by matching their horizontal and vertical gaps with the transverse coherence lengths of the beamline 60 μm (horizontally) and 235 μm (vertically) before the FZP). The intensity distribution around the **111** Pt reflection was measured in a coplanar diffraction geometry with the sample surface mounted horizontally. The scattered X-rays were detected using a two-dimensional (2D) Maxipix pixel detector[36] (516 × 516 pixels of 55 μm). The sample was mounted on a fast *xyz* piezoelectric stage with a lateral stroke of 100 μm and a resolution of 2 nm, sitting on a hexapod that was mounted on a (3 + 2 circles) goniometer. At the P10 beamline of PETRA III synchrotron at DESY, the BCDI experiment was performed at a beam energy of 8 keV (wavelength of 1.55 Å). The beam size was focused down to 0.9 μm (vertically) × 1.1 μm (horizontally) using Be compound refractive lenses. The sample was mounted in a dedicated water-cooled gas-flow chamber with the substrate surface oriented in the horizontal plane on a high-precision (1 μm) XYZ-stage that was mounted on a 6-circle Huber diffractometer. The diffracted beam was recorded with a 2D EIGER 4 M photon-counting detector (2070 × 2167 pixels with pixel size of 75 μm × 75 μm) positioned on the detector arm at a distance of 1.839 m. We measure the **111** Pt Bragg reflection in three-dimensions by rotating the particle around the Bragg angle (20°) through 3°, in steps of 0.012°. The detector was positioned at an out-of-plane of 39.26°.

Phase Retrieval. Phase retrieval was carried out on the raw diffracted intensity data using PyNX package,[37] imposing at each iteration that the calculated Fourier intensity of the guessed object agrees with the measured data. Defective pixels for experimental data and gaps in the detector were masked and were not used for imposing the reciprocal space constraint mentioned above. The initial support, which is the constraint in real space, was estimated from the autocorrelation of the diffraction intensity. A series of 1400 Relaxed Averaged Alternating Reflections (RAAR[38]) plus 200 Error-Reduction (ER[39]) steps including shrink wrap algorithm[40] were used. The phasing process included a partial coherence algorithm to account for the partially incoherent incoming wavefront.[41] The reconstruction was then corrected for refraction and absorption, the small size of the particles ensuring that dynamical diffraction effects could be neglected.[42] After removing the phase ramp and phase offset,[43] the data was finally interpolated onto an orthogonal grid for easier visualization.

AUTHOR INFORMATION

Corresponding Author

Marie-Ingrid Richard − *Univ. Grenoble Alpes, CEA Grenoble, IRIG/MEM/NRX, Grenoble 38054, France; ESRF - The European Synchrotron, Grenoble 38000, France;* orcid.org/0000-0002-8172-3141; Email: mrichard@esrf.fr

Authors

Stéphane Labat − *Aix Marseille Université, CNRS, Université de Toulon, 13397 Marseille, France*

Maxime Dupraz − *Univ. Grenoble Alpes,, CEA Grenoble, NRX, 38000 Grenoble, France; ESRF - The European Synchrotron, Grenoble 38000, France*

Jérôme Carnis − *Univ. Grenoble Alpes, CEA Grenoble, IRIG/MEM/NRX, Grenoble 38054, France;* orcid.org/0000-0001-7270-6211

Lu Gao − *Laboratory for Inorganic Materials and Catalysis, Department of Chemical Engineering and Chemistry, Eindhoven University of Technology, 5600 MB Eindhoven, The Netherlands;* orcid.org/0000-0002-7127-9980

Michaël Texier − *Aix Marseille Université, CNRS, Université de Toulon, 13397 Marseille, France;* orcid.org/0000-0001-6999-7978

Ni Li − *Univ. Grenoble Alpes,, CEA Grenoble, NRX, 38000 Grenoble, France*

Longfei Wu − *Laboratory for Inorganic Materials and Catalysis, Department of Chemical Engineering and Chemistry, Eindhoven University of Technology, 5600 MB Eindhoven, The Netherlands;* orcid.org/0000-0001-6330-3613

Jan P. Hofmann − *Surface Science Laboratory, Department of Materials and Earth Sciences, Technical University of Darmstadt, 64287 Darmstadt, Germany;* orcid.org/0000-0002-5765-1096

Mor Levi − *Department of Materials Science and Engineering, Technion-Israel Institute of Technology, 3200003 Haifa, Israel*

Steven J. Leake − *ESRF - The European Synchrotron, Grenoble 38000, France*

Sergey Lazarev − *Deutsches Elektronen-Synchrotron (DESY), D-22607 Hamburg, Germany*

Michael Sprung − *Deutsches Elektronen-Synchrotron (DESY), D-22607 Hamburg, Germany*

Emiel J.M. Hensen − *Laboratory for Inorganic Materials and Catalysis, Department of Chemical Engineering and Chemistry, Eindhoven University of Technology, 5600 MB Eindhoven, The Netherlands;* orcid.org/0000-0002-9754-2417

Eugen Rabkin − *Department of Materials Science and Engineering, Technion-Israel Institute of Technology, 3200003 Haifa, Israel;* orcid.org/0000-0001-5545-1261

Olivier Thomas − *Aix Marseille Université, CNRS, Université de Toulon, 13397 Marseille, France*

Complete contact information is available at: https://pubs.acs.org/10.1021/acsnano.3c01306

Notes

The authors declare no competing financial interest.

https://doi.org/10.1021/acsnano.3c01306
ACS Nano XXXX, XXX, XXX−XXX

ACKNOWLEDGMENTS

The authors are grateful to ESRF (proposal HC4760) and PETRA (proposal 20180962EC) synchrotrons for allocating beamtime. The measurement was performed at the ID01 beamline of the European synchrotron (ESRF) and at the P10 beamline of the PETRA III synchrotron at DESY, a member of the Helmholtz Association (HGF). We thank the ID01 and P10 beamline staff for excellent support during the experiment. This project has received funding from the European Research Council (ERC) under the European Union's Horizon 2020 research and innovation programme (grant agreement No. 818823) and from the DINACS ANR project (ANR-21-CE08-0033-01). The research leading to this result has been supported by the project CALIPSOplus under the Grant Agreement 730872 from the EU Framework Programme for Research and Innovation HORIZON 2020. We also wish to thank the support by a grant from the Ministry of Science and Technology, Israel and from the Centre National de la Recherche Scientifique (CNRS), France.

REFERENCES

(1) Barrett, C. S.; Massalski, T. B. *Structure of Metals: Crystallographic Methods, Principles and Data*, 3rd ed.; Pergamon: Oxford, 1980.

(2) Hirth, J. P.; Lothe, J. *Theory of dislocations*, 2nd ed.; Krieger Pub. Co: Malabar, FL, 1992.

(3) Lacombe, P.; Beaujard, L. The Application of Etch Figures on Pure Aluminum (99.99%) to the Study of Some Micrographic Problems. *J. Inst. Metals* **1947**, *74*, 1.

(4) Le Hazif, R.; Poirer, J.-P. Cross-Slip on {110} Planes in Aluminum Single Crystals Compressed along ⟨100⟩ Axis. *Acta Metall.* **1975**, *23*, 865−871.

(5) Bhatr, R. T.; Thrower, P. A.; Bitler, W. R. Observations of {212} ⟨100⟩ slip system in face centered cubic austenitic stainless steel. *Scripta Metallurgica* **1976**, *10*, 19−24.

(6) McLean, M.; Mykura, H. Non-octahedral slip in platinum polycrystals. *Acta Metall.* **1965**, *13*, 376−378.

(7) Karnthaler, H. P. The study of glide on 001 planes in f.c.c. metals deformed at room temperature. *Philosophical Magazine A* **1978**, *38*, 141.

(8) Stevens, A. L.; Pope, L. E. Observations of secondary slip in impact-loaded aluminum single crystals(1). *Scripta Metallurgica* **1971**, *5*, 981−985.

(9) Lee, T. C.; Robertson, I. M.; Birnbaum, H. K. Anomalous slip in an FCC system. *Ultramicroscopy* **1989**, *29*, 212−216.

(10) Kinney, J. H.; Guinan, M. W. Computer simulation of surface effects on defect production in tungsten. *Philosophical Magazine A* **1982**, *46*, 789−800.

(11) Behrens, M.; Studt, F.; Kasatkin, I.; Kühl, S.; Hävecker, M.; Abild-Pedersen, F.; Zander, S.; Girgsdies, F.; Kurr, P.; Kniep, B.-L.; Tovar, M.; Fischer, R. W.; Nørskov, J. K.; Schlögl, R. The Active Site of Methanol Synthesis over $Cu/ZnO/Al_2O_3$ Industrial Catalysts. *Science* **2012**, *336*, 893.

(12) Ulvestad, A.; Singer, A.; Clark, J. N.; Cho, H. M.; Kim, J. W.; Harder, R.; Maser, J.; Meng, Y. S.; Shpyrko, O. G. Topological defect dynamics in operando battery nanoparticles. *Science* **2015**, *348*, 1344−1347.

(13) Nilsson Pingel, T.; Jørgensen, M.; Yankovich, A. B.; Grönbeck, H.; Olsson, E. Influence of atomic site-specific strain on catalytic activity of supported nanoparticles. *Nat. Commun.* **2018**, *9*, 2722.

(14) Robinson, I.; Harder, R. Coherent X-ray diffraction imaging of strain at the nanoscale. *Nat. Mater.* **2009**, *8*, 291−298.

(15) Ulvestad, A.; Singer, A.; Cho, H. M.; Clark, J. N.; Harder, R.; Maser, J.; Meng, Y. S.; Shpyrko, O. G. Single Particle Nanomechanics in Operando Batterie via Lensless Strain Mapping. *Nano Lett.* **2014**, *14*, 5123−5127.

(16) Labat, S.; Richard, M.-I.; Dupraz, M.; Gailhanou, M.; Beutier, G.; Verdier, M.; Mastropietro, F.; Cornelius, T. W.; Schülli, T. U.; Eymery, J.; Thomas, O. Inversion Domain Boundaries in GaN Wires Revealed by Coherent Bragg Imaging. *ACS Nano* **2015**, *9*, 9210−9216.

(17) Ulvestad, A.; Welland, M. J.; Collins, S. S. E.; Harder, R.; Maxey, E.; Wingert, J.; Singer, A.; Hy, S.; Mulvaney, P.; Zapol, P.; Shpyrko, O. G. Avalanching strain dynamics during the hydriding phase transformation in individual palladium nanoparticles. *Nat. Commun.* **2015**, *6*, 10092.

(18) Ulvestad, A.; Clark, J. N.; Harder, R.; Robinson, I. K.; Shpyrko, O. G. 3D Imaging of Twin Domain Defects in Gold Nanoparticles. *Nano Lett.* **2015**, *15*, 4066−4070.

(19) Yau, A.; Cha, W.; Kanan, M. W.; Stephenson, G. B.; Ulvestad, A. Bragg coherent diffractive imaging of single-grain defect dynamics in polycrystalline films. *Science* **2017**, *356*, 739−742.

(20) Tian, N.; Zhou, Z.-Y.; Sun, S.-G.; Ding, Y.; Lin Wang, Z. Synthesis of tetrahexahedral platinum nanocrystals with high-index facets and high electro-oxidation activity. *Science* **2007**, *316*, 732−735.

(21) Chapman, H. N.; Barty, A.; Marchesini, S.; Noy, A.; Hau-Riege, S. P.; Cui, C.; Howells, M. R.; Rosen, R.; He, H.; Spence, J. C.; et al. High-resolution ab initio three-dimensional x-ray diffraction microscopy. *J. Opt. Soc. Am. A* **2006**, *23*, 1179−1200.

(22) Cherukara, M. J.; Cha, W.; Harder, R. J. Anisotropic nano-scale resolution in 3D Bragg coherent diffraction imaging. *Appl. Phys. Lett.* **2018**, *113*, 203101.

(23) Hofmann, F.; Phillips, N. W.; Das, S.; Karamched, P.; Hughes, G. M.; Douglas, J.; Cha, W.; Liu, W. Nanoscale Imaging of the Full Strain Tensor of Specific Dislocations Extracted from a Bulk Sample. *Phys. Rev. Materials* **2020**, *4* (1), 013801.

(24) Ulvestad, A.; Menickelly, M.; Wild, S. M. Accurate, rapid identification of dislocation lines in coherent diffractive imaging via a min-max optimization formulation. *AIP Advances* **2018**, *8*, 015114.

(25) Clark, J. N.; Ihli, J.; Schenk, A. S.; Kim, Y.-Y.; Kulak, A. N.; Campbell, J. M.; Nisbet, G.; Meldrum, F. C.; Robinson, I. K. Three-dimensional imaging of dislocation propagation during crystal growth and dissolution. *Nat. Mater.* **2015**, *14*, 780−784.

(26) Ulvestad, A.; Nashed, Y.; Beutier, G.; Verdier, M.; Hruszkewycz, S. O.; Dupraz, M. Identifying Defects with Guided Algorithms in Bragg Coherent Diffractive Imaging. *Sci. Rep.* **2017**, *7*, 9920.

(27) Steeds, J. W. Dislocation arrangement in copper single crystals as a function of strain. *Proceedings of the Royal Society of London. Series A. Mathematical and Physical Sciences* **1966**, *292*, 343−373.

(28) Williams, D. B.; Carter, C. B. *Transmission Electron Microscopy: A Textbook for Materials Science*; Plenum Press: New York, 1996.

(29) Hofmann, F.; Tarleton, E.; Harder, R. J.; Phillips, N. W.; Ma, P.-W.; Clark, J. N.; Robinson, I. K.; Abbey, B.; Liu, W.; Beck, C. E. 3D lattice distortions and defect structures in ion-implanted nano-crystals. *Sci. Rep.* **2017**, *7*, 45993.

(30) Pichaud, B.; Minari, F. Cross-slip at very low stresses in highly perfect Cu crystals. *Philos. Mag.* **1976**, *34*, 1121−1128.

(31) Pichaud, B.; Minari, F. Further topographic observations of zigzag stress-induced dislocations in copper crystals. *Philosophical Magazine A* **1979**, *40*, 121−124.

(32) Pichaud, B.; Minari, F. {110} Slip in copper slightly deformed at room temperature. *Scripta Metallurgica* **1980**, *14*, 1171−1174.

(33) Martin, J.; Caillard, D. The importance of noncompact slip in some close-packed metallic structures. *Zeitschrift für metallkunde* **1993**, *84*, 867−873.

(34) Caillard, D.; Martin, J. Some aspects of cross-slip mechanisms in metals and alloys. *J. Phys. (Paris)* **1989**, *50*, 2455−2473.

(35) Kalsar, R.; Madhavan, R.; Suwas, S. Texture evolution in platinum: the role of non-octahedral slip. *Philosophical Magazine Letters* **2021**, *101*, 360−369.

(36) Ponchut, C.; Rigal, J. M.; Clément, J.; Papillon, E.; Homs, A.; Petitdemange, S. MAXIPIX, a fast readout photon-counting X-ray area detector for synchrotron applications. *J. Inst.* **2011**, *6*, C01069.

https://doi.org/10.1021/acsnano.3c01306
ACS Nano XXXX, XXX, XXX−XXX

(37) Mandula, O.; Elzo Aizarna, M.; Eymery, J.; Burghammer, M.; Favre-Nicolin, V. *PyNX.Ptycho*: a computing library for X-ray coherent diffraction imaging of nanostructures. *J. Appl. Crystallogr.* **2016**, *49*, 1842−1848.
(38) Luke, D. R. Relaxed averaged alternating reflections for diffraction imaging. *Inverse Problems* **2005**, *21*, 37−50.
(39) Fienup, J. R. Reconstruction of an object from the modulus of its Fourier transform. *Opt. Lett., OL* **1978**, *3*, 27−29.
(40) Marchesini, S.; He, H.; Chapman, H. N.; Hau-Riege, S. P.; Noy, A.; Howells, M. R.; Weierstall, U.; Spence, J. C. H. X-ray image reconstruction from a diffraction pattern alone. *Phys. Rev. B* **2003**, *68*, 140101.
(41) Clark, J. N.; Huang, X.; Harder, R.; Robinson, I. K. High-resolution three-dimensional partially coherent diffraction imaging. *Nat. Commun.* **2012**, *3*, 993.
(42) Hu, W.; Huang, X.; Yan, H. Dynamic diffraction artefacts in Bragg coherent diffractive imaging. *J. Appl. Crystallogr.* **2018**, *51*, 167−174.
(43) Carnis, J. *BCDI Python package*, version 0.0.5, 2019. See the following: https://github.com/carnisj/bcdi.

https://doi.org/10.1021/acsnano.3c01306
ACS Nano XXXX, XXX, XXX−XXX